

Coherent radar imaging using Capon's method

Robert D. Palmer, Sridhar Gopalam, and Tian-You Yu

Department of Electrical Engineering and Center for Electro-Optics
University of Nebraska, Lincoln

Shoichiro Fukao

Radio Atmospheric Science Center, Kyoto University, Kyoto, Japan

Abstract. A linearly constrained mathematical formulation is provided for the problem of coherent radar imaging. In contrast to studies of field-aligned irregularities in the ionosphere, where the technique has previously been applied, lower atmospheric imaging is complicated by the fact that the scattering structures are not aligned along any single baseline. As a result, a two-dimensional generalization of the brightness distribution was required. It is shown that Fourier-based imaging is a special case of this general formulation. Furthermore, an imaging technique based on constrained optimization is introduced and shown to exhibit higher resolution and resistance to interfering signals. These techniques were applied to data from the middle and upper atmosphere radar in Shigaraki, Japan. The experiment was conducted during the Baiu season, which is characterized by significant precipitation events.

1. Introduction

Coherent radar imaging is a term which can be used to describe various array processing algorithms whereby signals from spatially separated sensors are processed in order to focus the receiver's sensitivity in particular directions [Johnson and Dudgeon, 1993]. This recently developed method is an outgrowth of the radar interferometric (RI) technique [Woodman, 1971] and has the potential to unravel the inherent ambiguities between temporal and spatial dimensions when using single-station observational instruments. It should be noted that the RI technique has also been termed spatial interferometry (SI) in the literature. Vertically pointing radars can typically be used to observe wind and reflectivity field dynamics as various meteorological events pass over the observation site. However, vertical wind shear, in both direction and magnitude, cause difficulties in the interpretation of resulting range time intensity plots. Imaging has the capability of creating an instantaneous "picture" of the atmosphere

within the beam of the radar. Therefore no ambiguities exist between the temporal and spatial scales.

The first application of true imaging was made by Kudeki and Sürücü [1991] for observations of the equatorial electrojet above the Jicamarca Radio Observatory in Peru. It is interesting to note that this Fourier-based technique is a generalization of the poststatistic steering (PSS) method, which has been used for wind field measurements [Kudeki and Woodman, 1990; Palmer *et al.*, 1993]. In addition, Van Baelen *et al.* [1991] used postset beam steering [Röttger and Ierkic, 1985], which is an equivalent time domain method, for two-dimensional imaging of the lower atmosphere. Although these straightforward techniques have been developed, little effort has been put forth to investigate the wealth of knowledge in more generalized imaging methods. An interesting exception is the work of Hysell [1996] and Hysell and Woodman [1997], in which the maximum entropy method was applied to the imaging problem. This technique has been shown to exhibit higher resolution than Fourier-based techniques. A general review paper in the area of imaging has also been recently published [Woodman, 1997]. In addition to maximum entropy, many previously developed algorithms exist that exhibit significant advantages in terms of

Copyright 1998 by the American Geophysical Union.

Paper number 98RS02200.

0048-6604/98/98RS-02200\$11.00

resolution and interference rejection. For example, Capon's method [Capon, 1969] has been shown to be extremely robust and has the potential to reduce effects from interfering signals such as ground clutter or the biasing effects of aspect sensitivity. The present work provides results from the application of Capon imaging for the study of clear-air turbulence (CAT) and a precipitation event associated with the Baiu season in Japan [e.g., Fukao *et al.*, 1988; Yamanaka *et al.*, 1996].

Scanning meteorological radars are usually used for the study of formation of storms. Under typical conditions, however, the relatively short wavelength (~ 10 cm) of these radars limits the observations to the actual precipitating particles, such as liquid water and ice crystals. These hydrometeors do not necessarily follow the vertical motion of the wind field especially during heavy precipitation. Furthermore, it has been shown that these particles do not perfectly trace even the horizontal flow [Chu *et al.*, 1997]. Meteorological radars, with their short wavelengths, typically cannot be used to observe the movements of the wind field, but only the motion of the hydrometeors. In contrast, mesosphere-stratosphere-troposphere (MST) radars are designed with wavelengths of the order of meters, resulting in the ability to observe the wind field. In addition, MST radars can be used to simultaneously observe scatter from hydrometeors [Wakasugi *et al.*, 1987; Gossard *et al.*, 1990]. Therefore MST radars are an ideal instrument for the study of the kinematics and microphysical processes involved in the formation and growth of both convective and stratiform precipitation. On the other hand, the longer wavelengths of MST radars cause wider beam widths and therefore worse angular resolution. Coherent radar imaging holds tremendous promise for increasing the angular resolution of these measurements.

Another disadvantage of meteorological radars is that they typically produce two-dimensional cross sections of reflectivity and radial velocity through a storm system. Interpretation of these "slices" of an inherently three-dimensional structure, such as a convective storm system, can be difficult and sometimes impossible. In fact, Yuter and Houze [1995, p. 1937] stated that "A method is needed that will overcome the limitations of cross sections, identify the salient ensemble properties of the storm, and reveal how these properties change as the storm evolves." The imaging algorithms currently under in-

vestigation can provide a three-dimensional view inside a precipitating cloud system, eliminating temporal and spatial scale ambiguities. By using contiguous data sets, animations of the three-dimensional structure can be generated providing the chance to study storm evolution. Moreover, Doppler sorting can be used with these imaging techniques providing the means to separate signals corresponding to various Doppler velocities. As mentioned earlier, hydrometeors do not necessarily follow the wind field and actually have a fall speed proportional to their size, if vertical air motion effects have been removed. Therefore imaging methods can be used to sort a precipitating structure according to three-dimensional position, fall speed, and time. Such a multidimensional view of the atmosphere will provide a wealth of information concerning the formation of these systems, including cloud structure, growth regions, and the distribution of various size hydrometeors within the cloud boundaries.

Section 2 provides the mathematical generalization of coherent radar imaging. Preliminary results are presented in subsequent sections illustrating the usefulness of the technique for imaging of CAT and precipitation.

2. Coherent Radar Imaging

2.1. Mathematical Problem Statement

As discussed previously, imaging techniques basically attempt to create a picture of the reflectivity structure, or brightness distribution, within the transmit beam of the radar. This map can be created vertically through the normal gating procedure used with most atmospheric radars. Horizontal maps of the brightness distribution are usually obtained in a crude manner through beam steering, which is typically limited to a small number of directions using phased-array antenna systems. This coarse sampling of the brightness distribution does not allow the detailed study of the fine structure and dynamics of the atmosphere.

Just as the signals from the elements of a phased-array antenna system are combined in order to steer the beam in certain directions, recently developed imaging techniques attempt to combine signals from a finite set of receiving arrays with various types of optimality constraints. In general, one would like to estimate the brightness in the direction of the wavenumber vector \mathbf{k} by combining the signals

from n receivers. This configuration is illustrated in Figure 1, with the wavenumber vector defined as $\mathbf{k} = (2\pi/\lambda) [\sin \theta \sin \phi \quad \sin \theta \cos \phi \quad \cos \theta]$, where θ and ϕ are the zenith and azimuth angles, respectively. A horizontal map of the brightness could be obtained by varying \mathbf{k} over an appropriate region of the sky. Since \mathbf{k} is varied in software, any number of sample points could be obtained. Of course, the resolution of the map ultimately depends on the length of the baselines and the method with which the n signals are combined.

Let $\mathbf{s}(t)$ represent a column vector containing the signals from the n receivers. Our task is to determine an optimal method of combining the elements of $\mathbf{s}(t)$. We will choose to combine the signals by a simple linear filter, where the column vector of constant coefficients will be denoted by \mathbf{w} and the scalar output of the filter $y(t)$ will be given by the following expression:

$$y(t) = \mathbf{w}^\dagger \mathbf{s}(t) \quad (1)$$

where the dagger represents the Hermitian (conjugate transpose) operator. It should be noted that \mathbf{w} will undoubtedly depend on the wavenumber vector \mathbf{k} . Assuming the output of the filter is wide sense stationary, the autocorrelation function of $y(t)$ has the following form:

$$R_y(\tau) = \langle y(t + \tau) y^*(t) \rangle \quad (2)$$

After appropriate substitution, the autocorrelation function takes on the following matrix form:

$$R_y(\tau) = \mathbf{w}^\dagger \mathbf{R}(\tau) \mathbf{w} \quad (3)$$

where $\mathbf{R}(\tau)$ is the correlation matrix of $\mathbf{s}(t)$. By taking the Fourier transform and normalizing the result, we arrive at the brightness distribution, where the dependence on \mathbf{k} is now explicitly shown.

$$B(\mathbf{k}, f) = \mathbf{w}^\dagger \mathbf{V}(f) \mathbf{w} \quad (4)$$

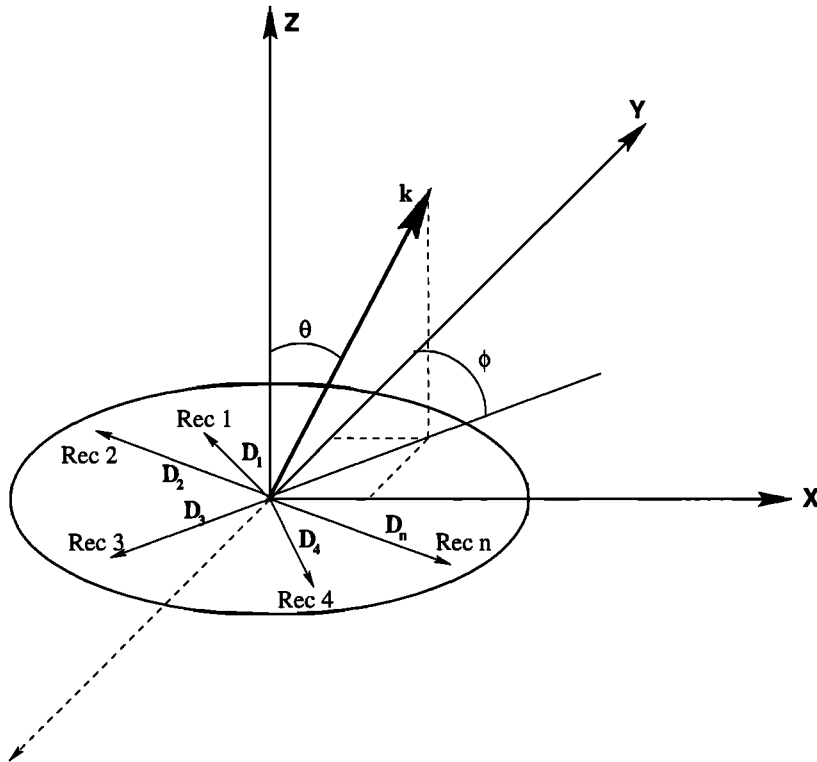


Figure 1. Shown is a general configuration for an interferometry system with n receivers. The vector \mathbf{k} represents the wavenumber vector with zenith and azimuth angles of θ and ϕ , respectively. Vectors representing the center of each receiving array are denoted by \mathbf{D}_i for receiver i .

The normalized cross-spectral matrix of the n received signals is denoted by $\mathbf{V}(f)$ and has the following form:

$$\mathbf{V}(f) = \begin{bmatrix} V_{11}(f) & V_{12}(f) & \dots & V_{1n}(f) \\ V_{21}(f) & V_{22}(f) & \dots & V_{2n}(f) \\ \vdots & \vdots & \ddots & \vdots \\ V_{n1}(f) & V_{n2}(f) & \dots & V_{nn}(f) \end{bmatrix} \quad (5)$$

where $V_{ij}(f)$ is the normalized cross spectrum between the signals from receivers i and j , which is also termed the visibility spectrum [Kudeki and Sürücü, 1991]. The normalization is calculated at each frequency and is obtained from the following equation:

$$V_{ij}(f) = \frac{\langle S_i(f) S_j^*(f) \rangle}{\sqrt{\langle |S_i(f)|^2 \rangle \langle |S_j(f)|^2 \rangle}} \quad (6)$$

where $S_i(f)$ is the Fourier transform of the coherently detected signal from receiver i . The magnitude of $V_{ij}(f)$ is typically termed the coherence. It should be emphasized that $\mathbf{V}(f)$ has a dependence on temporal frequency f . Therefore a separate estimate of brightness distribution can be calculated for each Doppler velocity. The definition of brightness distribution given in (4) is completely general for any linear combination of the n signals. The ultimate task is to determine the optimal weight vector \mathbf{w} in order to estimate the brightness in the direction of \mathbf{k} .

2.2. Fourier-Based Imaging

Signals from the elements of a phased-array antenna system are combined with appropriate phase shifts in order to steer the beam in various directions. This simple method can also be accomplished for the general configuration described in the previous section, resulting in the PSS technique [Kudeki and Woodman, 1990; Palmer et al., 1990].

By defining the weight vector in the following manner, the appropriate phase shifts can be introduced in order to steer the beam in the direction of \mathbf{k} .

$$\mathbf{w}_F = [e^{j\mathbf{k} \cdot \mathbf{D}_1} \quad e^{j\mathbf{k} \cdot \mathbf{D}_2} \quad \dots \quad e^{j\mathbf{k} \cdot \mathbf{D}_n}]^T \quad (7)$$

By substitution of (7) into (4), we arrive at the following form of the brightness distribution:

$$\begin{aligned} B_F(\mathbf{k}, f) = & V_{11} + V_{22} + \dots + V_{nn} \\ & + 2\text{Re}\{V_{12}e^{-j\mathbf{k} \cdot (\mathbf{D}_1 - \mathbf{D}_2)}\} + \dots \\ & \quad 2\text{Re}\{V_{1n}e^{-j\mathbf{k} \cdot (\mathbf{D}_1 - \mathbf{D}_n)}\} \\ & + 2\text{Re}\{V_{23}e^{-j\mathbf{k} \cdot (\mathbf{D}_2 - \mathbf{D}_3)}\} + \dots \\ & \quad 2\text{Re}\{V_{2n}e^{-j\mathbf{k} \cdot (\mathbf{D}_2 - \mathbf{D}_n)}\} \\ & \vdots \\ & + 2\text{Re}\{V_{n-1n}e^{-j\mathbf{k} \cdot (\mathbf{D}_{n-1} - \mathbf{D}_n)}\} \end{aligned} \quad (8)$$

which is an n -receiver generalization of the results given by Kudeki and Woodman [1990] for the two-receiver case and by Palmer et al. [1990] for the three-receiver case. From this point in the text, note that the dependence of the spectra on f has been omitted for notational convenience.

2.3. Capon Imaging

Although the Fourier-based imaging techniques have had some success, an abundance of sophisticated algorithms have been developed for applications such as radio astronomy, seismic exploration, and acoustic array processing. One such algorithm is termed Capon's method but is also referred to as the minimum variance method, for reasons that will become apparent in the next paragraph [Capon, 1969]. The technique was first developed for two-dimensional imaging of subterranean structures, using signals obtained from a seismic array.

The resolution of Fourier-based imaging is limited by the frequency response of the weight vector. Since \mathbf{w}_F has only phase shift terms, the magnitude response has the standard form of the sinc function, which possesses well-known main lobe and sidelobe characteristics. An obvious question is whether there might exist a more clever choice of the weight vector \mathbf{w} , which could improve the resolution and sidelobe characteristics. The idea proposed by Capon was to define a constrained optimization problem, where the goal would be to find the weight vector \mathbf{w} which minimizes the output power of the linear filter defined in (1). Equivalently, the brightness distribution defined in (4) could be minimized for each frequency. This would have the result of reducing the sidelobe effects, which hamper Fourier-based imaging. However, we cannot simply minimize $B(\mathbf{k}, f)$ since the optimal choice would be to choose \mathbf{w} to be the null vector. The minimization must be constrained such that the frequency response of \mathbf{w} is unity in the desired direction of \mathbf{k} . The problem is stated mathematically in

the following manner:

$$\min_{\mathbf{w}} B(\mathbf{k}, f) \text{ subject to } \mathbf{e}^\dagger \mathbf{w} = 1 \quad (9)$$

where

$$\mathbf{e} = [e^{j\mathbf{k} \cdot \mathbf{D}_1} \quad e^{j\mathbf{k} \cdot \mathbf{D}_2} \quad \dots \quad e^{j\mathbf{k} \cdot \mathbf{D}_n}]^T \quad (10)$$

This constrained minimization problem can be solved using Lagrange methods. It is shown in the appendix that the resulting form of the brightness distribution is as follows.

$$B_C(\mathbf{k}, f) = \frac{1}{\mathbf{e}^\dagger \mathbf{V}^{-1} \mathbf{e}} \quad (11)$$

An example of possible beam patterns from the Fourier-based and Capon's methods is shown in Figure 2. Fourier-based imaging uses no information about the signal and therefore the beam pattern is independent of any interference. Since \mathbf{w}_C is chosen to minimize the output power of the filter, the sidelobe pattern in the direction of the interfering signal is reduced. It should be mentioned that this reduction is pro-

vided at the cost of increased sidelobes in directions without interference. Of course, this has no effect on the estimate of the brightness distribution. It can also be shown that Capon's method has better angular resolution than Fourier-based methods and is more robust than techniques based on autoregressive models [Kay, 1987].

3. Experimental Configuration

The results of the present study were obtained from a combined SI and Doppler beam swinging (DBS) experiment conducted on July 22, 1995, 1634-2200 LT, using the middle and upper atmosphere (MU) radar, located in Shigaraki, Japan [Fukao *et al.*, 1985ab]. The configuration used for the SI portion of the experiment will first be explained. Since the SI data were not initially intended for the application of imaging, the experimental configuration was not optimal. Overlapping receiving arrays and rather short baseline lengths shown in Figure 3b produced images with degraded resolution. In general, better resolution is obtained by using longer baseline

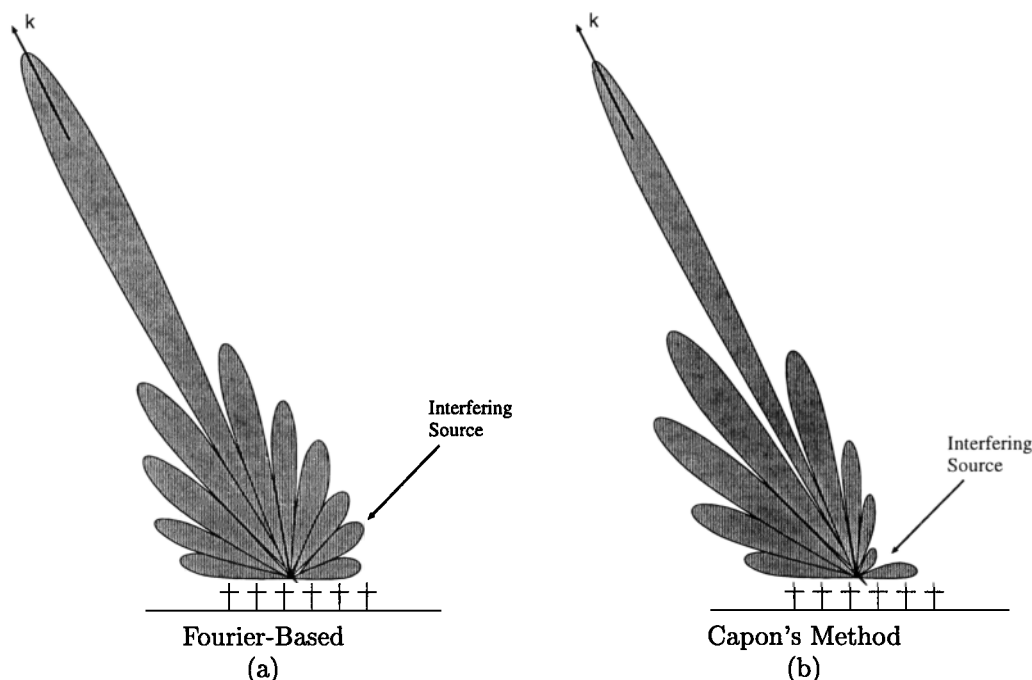


Figure 2. Depiction of possible resulting beam patterns using (a) Fourier-based and (b) Capon's imaging algorithms. Notice that the sidelobes of the pattern from Capon's method are adaptively reduced in the direction of the interfering source, which could represent ground clutter or simply the aspect sensitivity of the atmosphere, for example.

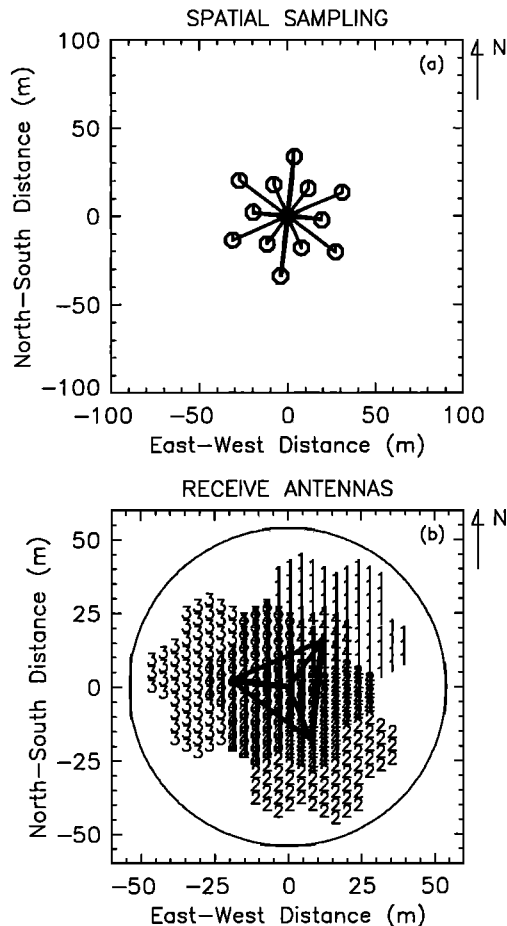


Figure 3. The locations of the individual antennas for this experimental configuration are shown in (b), where the numbers represent the receiver to which the antenna signal is fed. The three outer receivers form an equilateral triangle with separation of 33.97 m. The fourth receiver was placed at the center of the array with a separation of 19.62 m from the other three. The spatial sampling resulting from the receiver locations is depicted in (a).

lengths. In this particular configuration, however, the maximum distance between any two receivers was only 33.97 m, and the minimum distance was 19.62 m, resulting in aliasing angles of $\pm 5.44^\circ$ and $\pm 9.42^\circ$, respectively, along these baselines. It should be noted that two-dimensional, spatial aliasing is more complicated than the single-baseline case and involves the angles at which the various baselines constructively interfere. As a result, the angles at

which two-dimensional images repeat due to aliasing are always at least as large as for the single baseline case. For transmission, the entire MU radar array was used, which has a one-way, half-power beam width of only $\pm 1.8^\circ$. As a result, any possibility of angular aliasing was essentially eliminated by the transmit beam. The resulting spatial sampling for the receiver configuration is shown in Figure 3a. These vectors simply represent the lengths and azimuth angles of each baseline and provide a view of how well the ground diffraction pattern is sampled. Although the current receiver configuration provides rather poor angular resolution due to the short baseline lengths, no two baselines are redundant, resulting in a more uniform spatial sampling. Future experiments are currently planned to improve the angular resolution by configuring the receiving arrays with the longest possible baseline lengths without redundancy. Considerations are also being made for the construction of additional receivers, making possible much more flexible imaging experiments. Currently, the MU radar has only four receivers, which can be connected to any of the 25 array groups.

The interpulse period (IPP) for the SI data was set to 400 μs with 256 coherent integrations, resulting in an effective sampling time of 0.1024 s. The corresponding aliasing velocity is 15.75 m s^{-1} , which was more than adequate to prevent temporal aliasing since the transmit beam was directed only vertically. Transmitted pulses of 2- μs length were not coded since the sampled ranges of 0.5–9.8 km precluded their use. Range gating was performed every 300 m, producing 32 gates over the desired range. Data consisting of 256 samples were recorded on magnetic tape approximately every 27 s and was continued for 30 records. The SI data were then processed off-line using a standard fast Fourier transform algorithm with no spectral windowing to produce the cross spectra. Incoherent integration of 10 records was performed and then used to produce the normalized cross-spectral matrix given in (5). Before normalization, the dc component of the various spectra was eliminated by linear interpolation. As a result of the incoherent integration, the images presented in the following section correspond to a time average of approximately 5 min.

The radar mode was alternated between the SI mode just described and a standard DBS mode, where 64 gates with spacing of 150 m were used to sample the range over 0.5–9.95 km. The DBS mode

used 1- μ s uncoded pulses and the IPP was again set to 400 μ s, but 16 coherent integrations were used in this case. Seventeen beam directions were used with zenith angles of 0°, 9°, and 20°. Azimuth angles were chosen at 45° intervals, resulting in eight beams for zenith angles of 9° and 20°. Since the MU radar system switches beam positions every IPP, the effective sampling time was 0.1088 s, corresponding to an aliasing velocity of 14.8 m s⁻¹. Using data sets consisting of 128 time series points, Doppler spectra were calculated on-line with no spectral windowing and six incoherent integrations. Ten records of these data, each consisting of 84 s, were recorded to magnetic tape. Then, the SI and DBS modes were alternated for the duration of the experiment, which was approximately 5.5 hours.

4. Preliminary Results

4.1. Doppler Beam Swinging

Using the DBS data, standard measurements were made of echo power and the wind field. These data are shown in Figure 4 in a time-height profile format. After an additional five incoherent integrations, each profile corresponds to an average time of approximately 7 min. The echo power from the vertical beam is shown in Figure 4a, while the zonal and meridional wind components are shown in Figures 4b and 4c, respectively. Notice the distinct reversal in the lower altitude meridional flow during the extent of the experiment. Bold lines are used to show the profiles corresponding to time 2121 LT, which is emphasized since this is the period closest to the time of the imaging results presented in the next section. A more detailed plot of the 2121 LT profile is provided in Figure 5, where a vertical change in the horizontal flow direction is more easily observed. A significant sheared region is seen in the range 2.0–3.5 km, above which the meridional flow reduces to approximately zero. Below this region, the wind is approximately southwesterly, while above, it changes to a westerly flow. This distinctive pattern will be used to help explain the results from the imaging experiment. The echo power is displayed in Figure 5b for the vertical beam and azimuthal averages of the off-vertical zenith angles, and the range squared dependence has not been removed. As expected, the sheared region (2.0–3.5 km) exhibits an isotropic behavior since the atmosphere is expected to be well mixed at these

altitudes. Above and below this region, aspect sensitivity is observed.

4.2. Horizontal Cross Sections

Both the Fourier-based and Capon imaging techniques were implemented for comparison. Using equations (8) and (11), images of the brightness distribution were obtained for zenith angles less than 4° and all possible Doppler velocities. As mentioned previously, the brightness distribution can be calculated for each Doppler frequency. Typically, an average brightness over some appropriate frequency range is obtained. For example, *Hysell* [1996] used an average over frequencies centered about zero since most of the observed signal strength existed in that range. However, it was mentioned that it might be advantageous to study the brightness distribution for different Doppler frequencies. Our data provide an interesting test case for this type of analysis since precipitation and clear-air echoes possess much different Doppler velocities and can be simultaneously observed at VHF wavelengths. This advantage will be exploited in the data presented in the next section. For the preliminary comparison, a frequency average over ± 1 m s⁻¹ was chosen as appropriate based on the observed spectral content.

Because of the abundance of information obtained from these imaging techniques, data presentation is a rather interesting problem. We have chosen to initially display the brightness distribution for each gate individually. Plate 1 presents an example from eight arbitrary ranges, which are denoted next to each pair of images. In each pair, the left image corresponds to the Fourier-based method, while the right image is obtained from Capon's method. The image intensity is normalized to the maximum brightness for each image individually and is presented on a linear scale. Red colors correspond to the highest brightness normalized to unity, while black represents no data. As mentioned previously, the transmit 3-dB beam width of the MU radar is 3.6°, essentially eliminating the possibility of angular aliasing. However, this also has the effect of reducing the statistical confidence for brightness estimates at larger zenith angles. Other biasing effects due to the transmit beam could possibly be removed with accurate knowledge of the actual beam pattern [Woodman, 1997]. The reader can view Plate 1 as a horizontal slice of the atmosphere at the ranges specified. Notice the improved resolution of Capon's method, where more detail is observed in

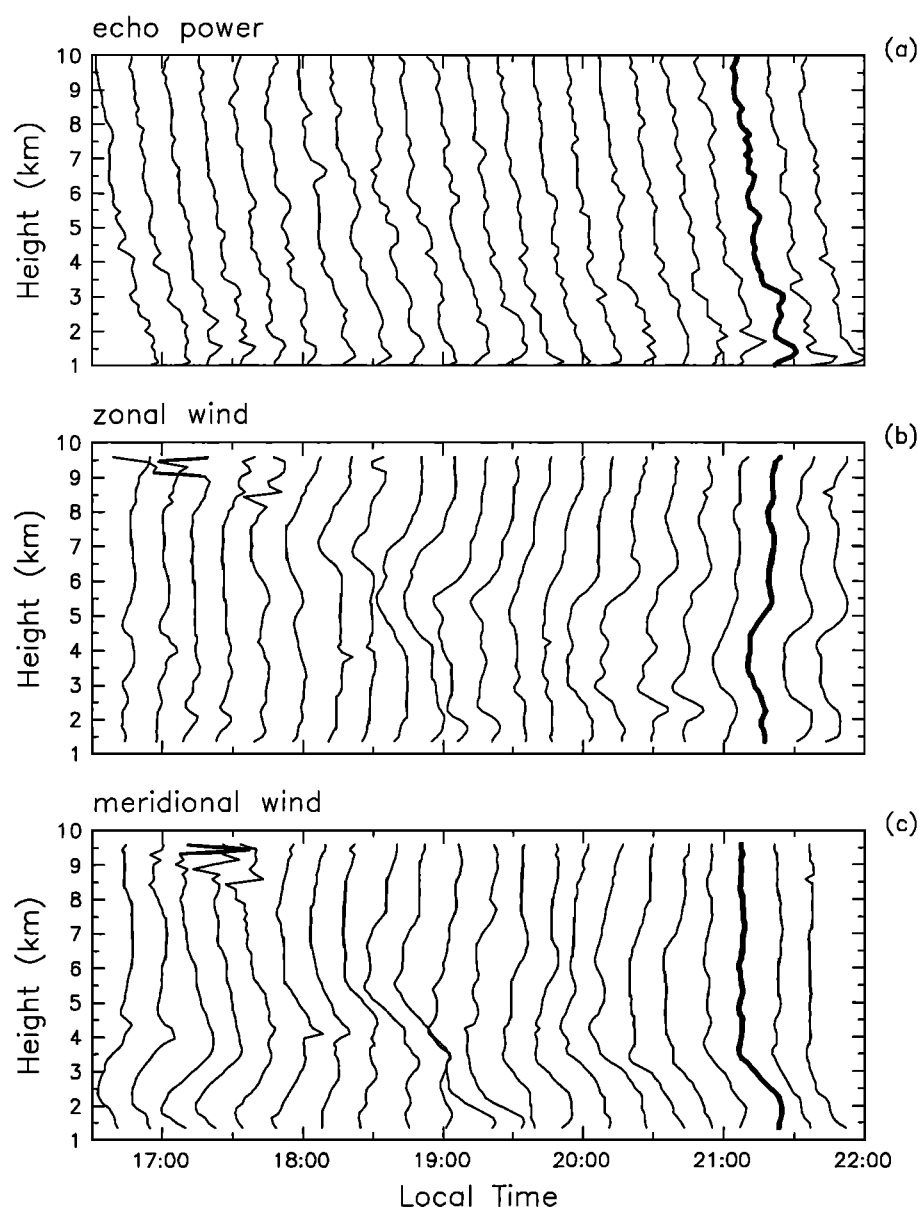


Figure 4. Time-height profiles of (a) echo power, (b) zonal wind, and (c) meridional wind, for the duration of the experiment. The profiles shown by the bold lines correspond to a time of 2121 LT. Data close to this time period will be used for examples of the imaging results.

the images, such as horizontal anisotropy. From the images, it can be seen that the peak in the brightness distribution can be shifted from vertical by as much as $\sim 1^\circ$, which compares well with angle-of-arrival measurements using standard SI techniques [Chau and Balsley, 1998]. Furthermore, because of the ef-

fect of the transmit beam pattern and the poor resolution of the Fourier-based method, the peak in the brightness distribution for this method is “pulled” toward zenith. Therefore the true atmospheric brightness is not obtained. Since Capon’s method typically produces a more narrow beam pattern, the effect of

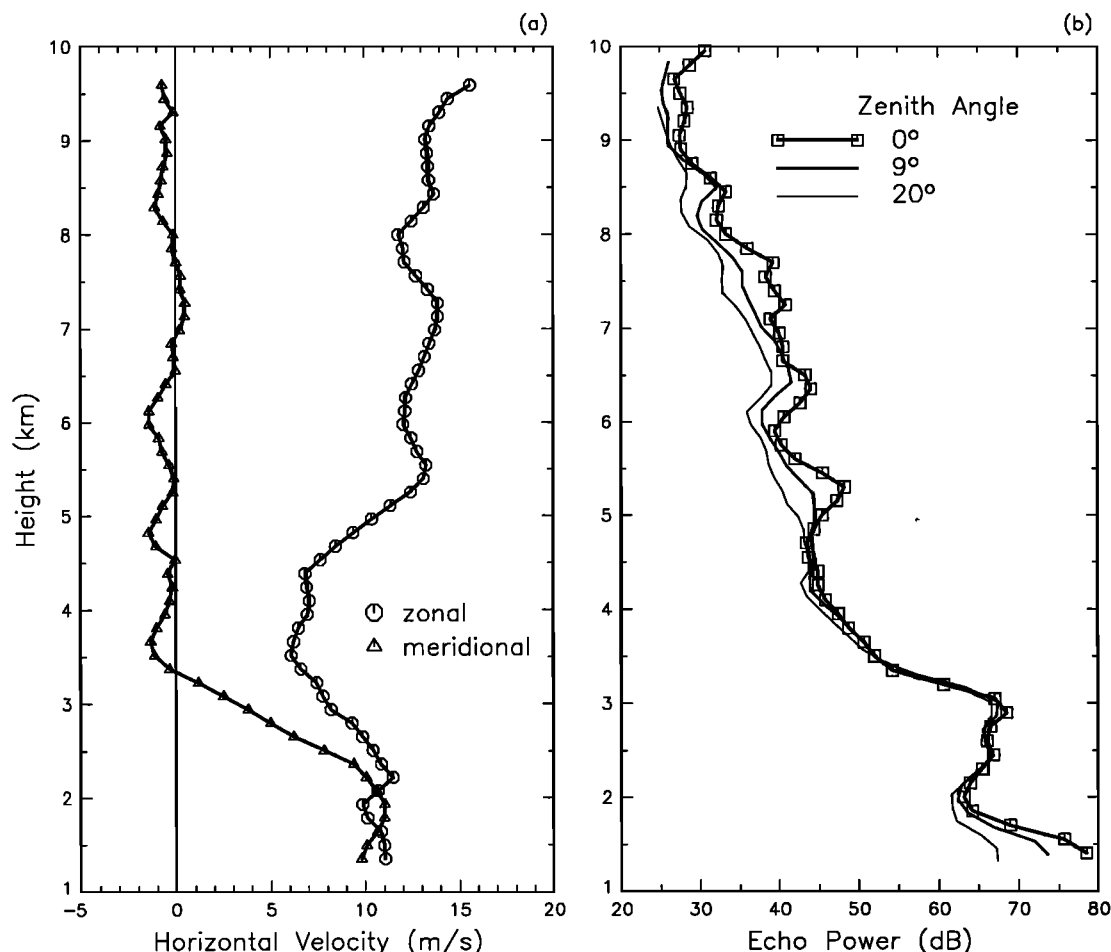


Figure 5. Detailed profiles from 2121 LT of (a) the horizontal wind field and (b) the echo power, from zenith angles of 0° , 9° , and 20° . Notice the isotropic behavior in the region of large vertical shear (2.0–3.5 km), where one would expect a well-mixed atmosphere. Another interesting feature is the approximate westerly wind above the sheared region, which will be used to explain characteristics of the imaging results.

the transmit beam is less significant. It should be emphasized that the images presented here are for zenith angles less than 4° . Therefore a direct comparison with the echo power profiles of Figure 5b is not possible, since the zenith angles of the DBS experiment are 0° , 9° , and 20° .

In order to test the frequency selectivity of coherent radar imaging, we have used Capon's method over two specific velocity ranges. The results are displayed in Plate 2 for the same altitudes of Plate 1. In this case, the left image corresponds to negative velocities, while the right image is averaged over pos-

itive velocities. For a horizontal flow, one would expect symmetry in the images along the direction of the wind vector. At the range of 1.4 km, for example, an approximate southwesterly wind was observed in Figure 5. As expected, the images have peaks which align approximately along the direction of the horizontal wind vector. Vertical wind would have the effect of shifting the images along the direction of the horizontal wind vector. Of course, wind field inhomogeneities would have an even more distorting effect on the images. For altitudes above 3.8 km, the images are aligned along the zonal direction, which

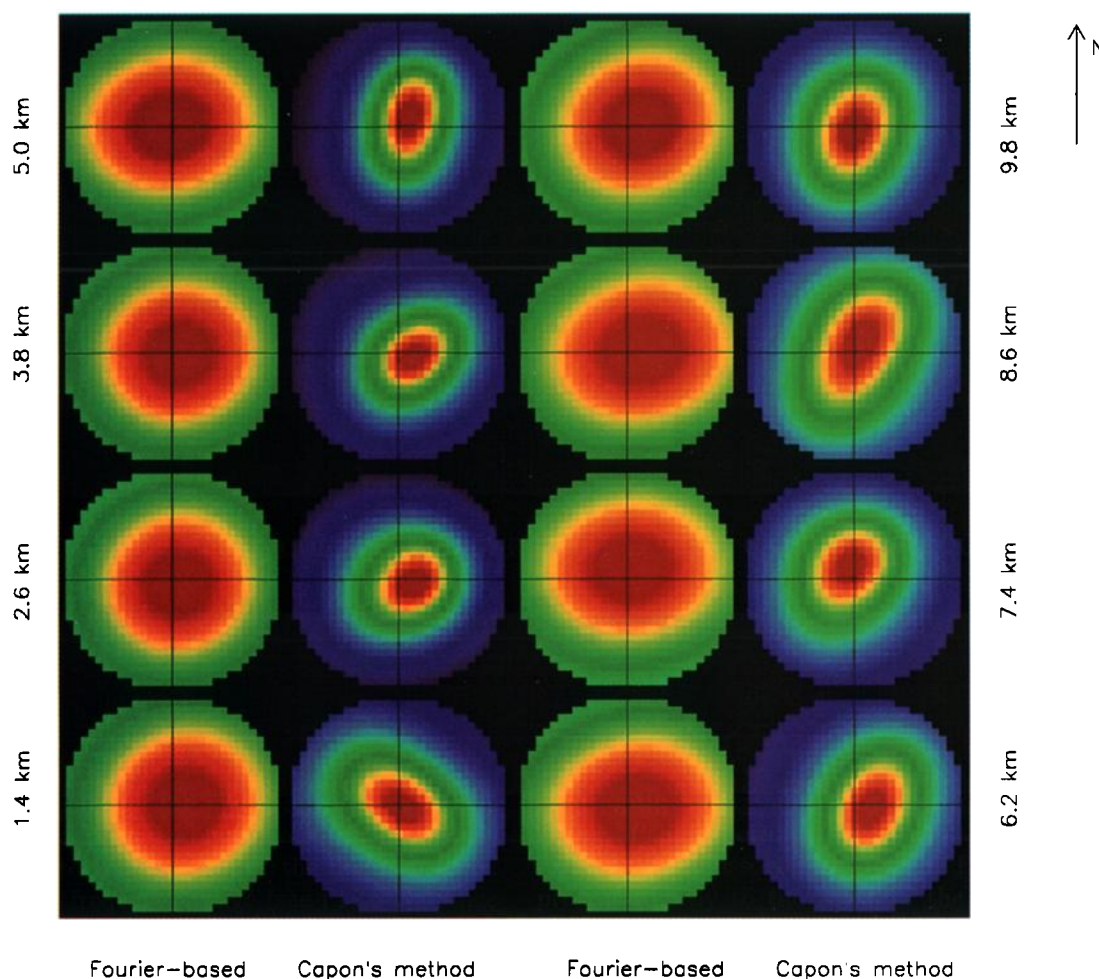


Plate 1. These images are of brightness distribution average over the velocity range $\pm 1 \text{ m s}^{-1}$ within $\pm 4^\circ$ above the middle and upper atmosphere (MU) radar site at eight arbitrary altitudes. Red colors correspond to highest brightness. As shown, images on the left and right of each pair were obtained using Fourier-based and Capon imaging techniques, respectively. Notice that Capon's method seems to exhibit better resolution than the Fourier-based method.

again corresponds to the approximate direction of the horizontal wind flow. It should be noted that the midpoint between the peaks of the images corresponding to positive and negative velocities should be equivalent to the location of the peak observed over the entire frequency range (see Plate 1). Since this is approximately the case, confidence is gained that the frequency selectivity capability of coherent radar imaging functions as expected.

4.3. Vertical Cross Sections

Synoptic surface maps show that for the entire duration of the experiment (5.5 hours), the stationary front typically associated with the Baiu season was present slightly to the north of the MU radar site in Shigaraki. Furthermore, light stratiform precipitation ($1\text{--}3 \text{ mm h}^{-1}$) was detected at the radar site during the experiment, which is shown in Figure 6.

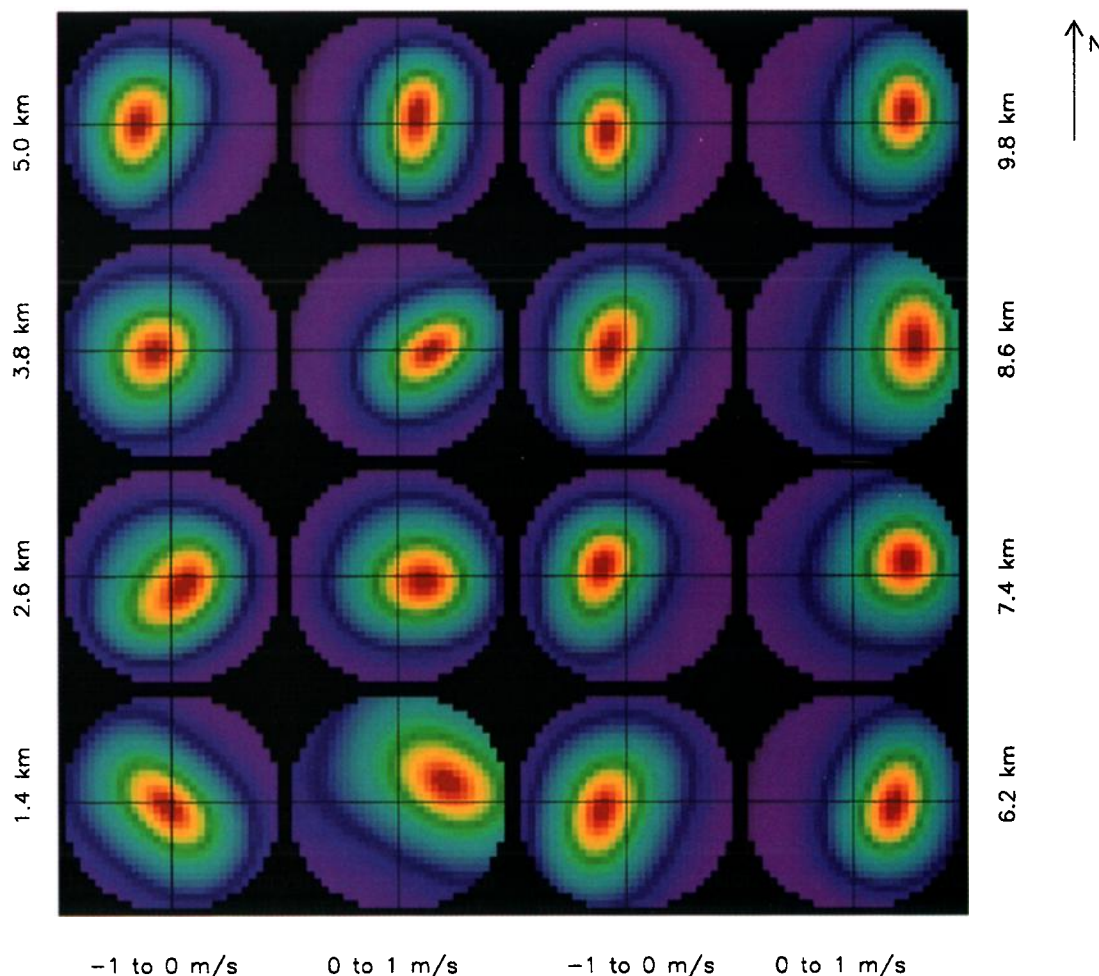


Plate 2. These images are a comparison of brightness distribution using Capon's method over two opposite velocity ranges and for the same altitudes as Plate 1. In each pair of images, the left corresponds to an average over negative velocities ($-1 \leftrightarrow 0 \text{ m s}^{-1}$), while the right represents positive velocities ($0 \leftrightarrow +1 \text{ m s}^{-1}$). Since the images correspond to opposite velocity ranges, symmetry should be expected along the direction of the wind vector.

Owing to the stratified nature of this type of precipitation, vertical cross sections of the atmosphere may be more illustrative of the power of the technique, than horizontal cross sections. Stratiform precipitation events associated with nimbostratus clouds are usually characterized by updrafts with much less magnitude than the terminal fall velocity of ice crystals ($1\text{--}2 \text{ m s}^{-1}$). Therefore ice crystals that form in the upper part of the cloud slowly fall toward Earth, increasing their size through deposition well above the freezing level. Just above the freezing level, aggregation and riming can occur, causing increased

size in the ice crystals. The "bright band" is a term used to describe the increase in meteorological radar reflectivity seen when the ice crystals begin to melt. The bright band has also been observed using MST radars [e.g., *Chilson et al.*, 1992].

Using the data described in the previous section, Capon's method has been used to image the stratiform precipitation event present during the experiment. A sequence of eight vertical cross sections of brightness distribution (along the zonal direction) is presented in Plate 3. The figure corresponds to a time of 1858 LT, which was chosen due to the rel-

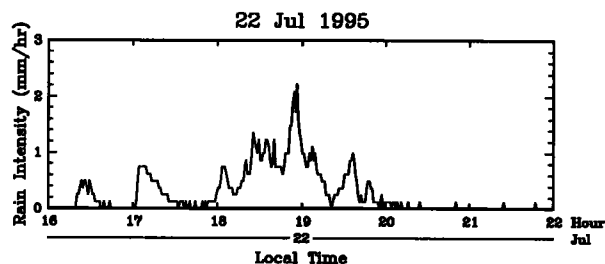


Figure 6. During the time of the experiment, stratiform precipitation was observed at the MU radar site. The precipitation intensity is in units of mm h^{-1} .

atively heavy precipitation rate shown in Figure 6.

The vertical axis represents a range from 1.4 to 9.8 km, while the horizontal axis for each panel corresponds to zenith angles within $\pm 4^\circ$. The leftmost panel presents the brightness distribution for downward radial velocities centered at 7 m s^{-1} , which would correspond to large, liquid, hydrometeors in stratiform precipitation. Notice that the red portions of the image (higher brightness) are near the surface and at small zenith angles. As mentioned previously, one would expect larger precipitation particles to exist nearer the surface in stratiform precipitation. The zenith angle dependence is caused by the transmit beam pattern. Above approximately 4 km, the image is not coherent, which exemplifies the lack of precipitation particles with a 7 m s^{-1} fall velocity. As an aside, it should be emphasized that

vertical images like the ones presented here would be extremely useful in the interpretation of convective precipitation. As the panels in Plate 3 are viewed from left to right, precipitation particles corresponding to progressively smaller fall velocities are imaged. As expected in a nimbostratus cloud, notice that the brightest altitudes move upward for smaller fall velocities. In addition, the tilt of the frontal surface as a function of height can be seen in the rightmost panel corresponding to the clear-air echo. It is interesting to note that the clear-air echo is not as bright as those due to precipitation. This is undoubtedly caused by the increased coherence in the precipitation echoes over that of the more random CAT signal.

5. Conclusions

A general mathematical construct has been presented for the case of two-dimensional coherent radar imaging. This generalization has placed the problem in terms of a linear filter interpretation, and it was shown that Fourier-based imaging [Kudeki and Sürücü, 1991] is a special case of this formulation. By adaptive minimization of the output power of the linear filter, we have applied Capon's method [Capon, 1969] to the problem of imaging CAT and a stratiform precipitation event associated with the Baiu season in Japan. Furthermore, Fourier-based imaging was implemented for comparison, which illustrated the robustness and higher resolution capabilities of Capon's method. Horizontal maps of brightness distribution demonstrated how coherent radar

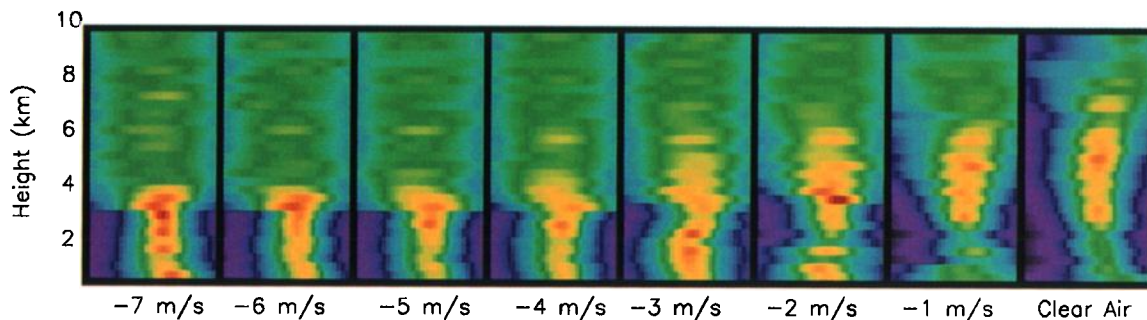


Plate 3. Shown is a sequence of eight vertical cross sections of brightness distribution, obtained using Capon imaging, due to precipitation particles of various fall velocities and clear-air turbulence along the zonal direction. The vertical axis range is from 1.4 to 9.8 km, while the horizontal scale of each image is zenith angle, with limits of $\pm 4^\circ$. From left to right, the eight panels correspond to brightness distribution for the Doppler radial velocity stated below each panel for a time of approximately 1858 LT.

imaging might be used to study anisotropy of turbulent structures. Vertical cross sections of brightness distribution exemplified the power of the technique for studies of stratiform precipitation.

Future work will include simulation studies of clear-air turbulence and precipitation. Many other multidimensional imaging techniques are available and should be thoroughly studied in order to find the ideal choice [e.g., Kay, 1987; Stoica and Moses, 1997]. Simulations can also be used to find optimal antenna configurations in terms of angular resolution and spatial aliasing considerations.

Appendix: Brightness Distribution Using Capon's Method

The equations governing Capon's imaging method are derived under the premise that it is desirable to minimize the brightness in all directions, with the exception of the desired direction of \mathbf{k} . This constrained minimization problem is stated mathematically in the following manner:

$$\min_{\mathbf{w}} B(\mathbf{k}, f) \text{ subject to } \mathbf{e}^\dagger \mathbf{w} = 1 \quad (\text{A1})$$

where

$$\mathbf{e} = [e^{j\mathbf{k} \cdot \mathbf{D}_1} \quad e^{j\mathbf{k} \cdot \mathbf{D}_2} \quad \dots \quad e^{j\mathbf{k} \cdot \mathbf{D}_n}]^T \quad (\text{A2})$$

The linear constraint term $\mathbf{e}^\dagger \mathbf{w}$ can be viewed as the spatial frequency response in the direction of \mathbf{k} .

This problem can be solved using standard Lagrange methods [Luenberger, 1984]. Using the general form of the brightness distribution given in (4), define the Lagrangian as follows:

$$L(\mathbf{w}, \gamma) = \mathbf{w}^\dagger \mathbf{V} \mathbf{w} + \gamma(\mathbf{e}^\dagger \mathbf{w} - 1) \quad (\text{A3})$$

where γ is the Lagrange multiplier. If \mathbf{V} is positive definite, the necessary and sufficient condition to solve the constrained minimization problem stated in (A1) is provided by the weight vector \mathbf{w} which satisfies the following equation:

$$\frac{d}{d\mathbf{w}} L(\mathbf{w}, \gamma) = 0 \quad (\text{A4})$$

Calculating this gradient, one arrives at the following equation:

$$2\mathbf{V}\mathbf{w} + \gamma\mathbf{e} = 0 \quad (\text{A5})$$

The weight vector which minimizes the Lagrangian is then given by the following, where a dependence on the Lagrange multiplier is shown.

$$\mathbf{w} = -\frac{\gamma}{2} \mathbf{V}^{-1} \mathbf{e} \quad (\text{A6})$$

After substitution of (A6) into the linear constraint $\mathbf{e}^\dagger \mathbf{w} = 1$, the Lagrange multiplier can be obtained.

$$\gamma = \frac{-2}{\mathbf{e}^\dagger \mathbf{V}^{-1} \mathbf{e}} \quad (\text{A7})$$

Finally, the optimal weight vector is found to have the following form:

$$\mathbf{w}_C = \frac{\mathbf{V}^{-1} \mathbf{e}}{\mathbf{e}^\dagger \mathbf{V}^{-1} \mathbf{e}} \quad (\text{A8})$$

The brightness distribution estimate using Capon's method is then obtained by substituting \mathbf{w}_C into (4), resulting in the following simple equation:

$$B_C(\mathbf{k}, f) = \frac{1}{\mathbf{e}^\dagger \mathbf{V}^{-1} \mathbf{e}} \quad (\text{A9})$$

It should be noted that the only assumption needed in the derivation is that \mathbf{V} is positive definite, which holds for the case of the cross-spectral matrix. The form of $B_C(\mathbf{k}, f)$ is totally general and can be applied to any data, irrespective of the expected structure of the brightness distribution.

Acknowledgments. S.G., R.D.P., and T.Y.Y. were supported by the Division of Atmospheric Sciences of the National Science Foundation through grant ATM 94-02021. The authors thank J. Chau and R. G. Roper for their helpful comments on the original manuscript. The MU radar belongs to and is operated by the Radio Atmospheric Science Center of Kyoto University.

References

- Baelen, J. S. V., A. D. Richmond, T. Tsuda, S. K. Avery, S. Kato, S. Fukao, and M. Yamamoto, Radar interferometry technique and anisotropy of the echo power distribution: First results, *Radio Sci.*, **26**, 1315–1326, 1991.
- Capon, J., High-resolution frequency-wavenumber spectrum analysis, *Proc. IEEE*, **57**, 1408–1419, 1969.
- Chau, J. L., and B. B. Balsley, Interpretation of angle-of-arrival measurements in the lower atmosphere using spaced antenna radar systems, *Radio Sci.*, **33**, 517–533, 1998.
- Chilson, P. B., R. D. Palmer, M. F. Larsen, C. W. Ulbrich, S. Fukao, M. Yamamoto, T. Tsuda, and S. Kato, First observations of precipitation with a spatial interferometer, *Geophys. Res. Lett.*, **19**, 2409–2412, 1992.
- Chu, Y.-H., T.-Y. Chen, and T.-H. Lin, An examination of the wind-driven effect on the drift of precipitation

- particles using the Chung-Li VHF radar, *Radio Sci.*, **32**, 957–966, 1997.
- Fukao, S., T. Sato, T. Tsuda, S. Kato, K. Wakasugi, and T. Makihira, The MU radar with an active phased array system, 1, Antenna and power amplifiers, *Radio Sci.*, **20**, 1155–1168, 1985a.
- Fukao, S., T. Tsuda, T. Sato, S. Kato, K. Wakasugi, and T. Makihira, The MU radar with an active phased array system, 2, In-house equipment, *Radio Sci.*, **20**, 1169–1176, 1985b.
- Fukao, S., M. D. Yamanaka, T. Sato, T. Tsuda, and S. Kato, Three-dimensional air motions over the Baiu front observed by a VHF-band Doppler radar: A case study, *Mon. Weather Rev.*, **116**, 281–292, 1988.
- Gossard, E. E., R. G. Strauch, and R. R. Rogers, Evolution of drop-size distribution in liquid precipitation observed by ground-based Doppler radar, *J. Atmos. Oceanic Technol.*, **7**, 815–818, 1990.
- Hysell, D. L., Radar imaging of equatorial *F* region irregularities with maximum entropy interferometry, *Radio Sci.*, **31**, 1567–1578, 1996.
- Hysell, D. L., and R. F. Woodman, Imaging coherent backscatter radar observations of topside equatorial spread *F*, *Radio Sci.*, **32**, 2309–2320, 1997.
- Johnson, D. H., and D. E. Dudgeon, *Array Signal Processing*, Prentice Hall, Englewood Cliffs, N. J., 1993.
- Kay, S., *Modern Spectral Estimation: Theory and Application*, Prentice-Hall, Englewood Cliffs, N. J., 1987.
- Kudeki, E., and F. Sürücü, Radar interferometric imaging of field-aligned plasma irregularities in the equatorial electrojet, *Geophys. Res. Lett.*, **18**, 41–44, 1991.
- Kudeki, E., and R. Woodman, A poststatistics steering technique for MST radar applications, *Radio Sci.*, **25**, 591–594, 1990.
- Luenberger, D. G., *Linear and Nonlinear Programming*, Addison-Wesley, Reading, Mass., 1984.
- Palmer, R. D., R. F. Woodman, S. Fukao, T. Tsuda, and S. Kato, Three-antenna poststatistic steering using the MU radar, *Radio Sci.*, **25**, 1105–1110, 1990.
- Palmer, R. D., M. F. Larsen, E. L. Sheppard, S. Fukao, M. Yamamoto, T. Tsuda, and S. Kato, Poststatistic steering wind estimation in the troposphere and lower stratosphere, *Radio Sci.*, **28**, 261–271, 1993.
- Röttger, J., and H. Ierke, Postset beam steering and interferometer applications of VHF radars to study winds, waves, and turbulence in the lower and middle atmosphere, *Radio Sci.*, **20**, 1461–1480, 1985.
- Stoica, P., and R. Moses, *Introduction to Spectral Analysis*, Prentice-Hall, Englewood Cliffs, N. J., 1997.
- Wakasugi, K., A. Mizutani, M. Matsuo, S. Fukao, and S. Kato, Further discussion on deriving drop-size distribution and vertical air velocities from VHF Doppler radar spectra, *J. Atmos. Oceanic Technol.*, **4**, 170–179, 1987.
- Woodman, R. F., Inclination of the geomagnetic field measured by an incoherent scatter technique, *J. Geophys. Res.*, **76**, 178–184, 1971.
- Woodman, R. F., Coherent radar imaging: Signal processing and statistical properties, *Radio Sci.*, **32**, 2372–2391, 1997.
- Yamanaka, M. D., S. Ogino, S. Kondo, T. Shimo-mai, S. Fukao, Y. Shibagaki, Y. Maekawa, and I. Takayabu, Inertio-gravity waves and subtropical multiple tropopauses: Vertical wavenumber spectra of wind and temperature observed by the MU radar, radiosondes and operational rawinsonde network, *J. Atmos. Sol. Terr. Phys.*, **58**, 785–805, 1996.
- Yuter, S. E., and J. R. A. Houze, Three-dimensional kinematic and microphysical evolution of Florida cumulonimbus, I, Spatial distribution of updrafts, downdrafts, and precipitation, *Mon. Weather Rev.*, **123**, 1921–1940, 1995.

S. Fukao, Radio Atmospheric Science Center, Kyoto University, Kyoto 611, Japan. (e-mail: fukao@kurasc.kyoto-u.ac.jp)

S. Gopalam, R. D. Palmer, and T.-Y. Yu, Department of Electrical Engineering, University of Nebraska, Lincoln, NE 68588-0511. (e-mail: gopalam@cig.mot.com; bpalmer@unlinfo.unl.edu; tian@doppler.unl.edu)

(Received May 18, 1998; revised June 24, 1998; accepted June 30, 1998.)